Applied Catalysis B: Environmental 254 (2019) 685–692

Contents lists available at ScienceDirect

Applied Catalysis B: Environmental

journal homepage: www.elsevier.com/locate/apcatb

Improving the electrochemical oxidation of formic acid by tuning the electronic properties of Pd-based bimetallic nanoparticles

Shuozhen Hu[a], Fanglin Che[b], Bita Khorasani[b], Mina Jeon[c], Chang Won Yoon[c], Jean-Sabin McEwen[b,d,e,f,g], Louis Scudiero[f], Su Ha[b,*]

[a] State Key Laboratory of Chemical Engineering, East China University of Science and Technology, Shanghai, 200237, China
[b] The Gene and Linda Voiland School of Chemical Engineering and Bioengineering, Washington State University, Pullman, WA, 99164, United States
[c] Fuel Cell Research Center, Korea Institute of Science and Technology, Seoul, 02792, Republic of Korea
[d] Institute for Integrated Catalysis, Pacific Northwest National Laboratory, Richland, WA, 99352, United States
[e] Department of Physics and Astronomy, Washington State University, Pullman, WA, 99164, United States
[f] Department of Chemistry, Washington State University, Pullman, WA, 99164, United States
[g] Department of Biological Systems Engineering, Washington State University, Pullman, WA, 99164, United States

ARTICLE INFO

Keywords:
Pd-based bimetallic nanoparticles
d-band center
Formic acid electrochemical oxidation
Volcano plot
DFT-based calculations

ABSTRACT

Pd-based bimetallic nanoparticles have superior electrochemical activity and stability for formic acid oxidation (FAO) than pure Pd. Previous DFT-based calculations show that the catalytic properties of the Pd surface could be altered by modifying its electronic properties. However, only a few experimental studies investigate how the electronic properties of Pd are modified by introducing various metals and how the resulting electronic perturbation affects its electrochemical activity and stability for FAO. Here, we demonstrate a correlation between electrochemistry and electronic properties for Pd-M bimetallic nanoparticles (M = Ru, Pt, Cu, Au, and Ag). The volcano shape relationship obtained between activity and *d*-band center values suggests that the electronic effects play a major role in modifying the surface electrochemical properties of Pd-M bimetallic nanoparticles for FAO. Among all the bimetallic catalysts investigated in this study, Pd-Pt/C and Pd-Cu/C with *d*-band center values of 2.58 eV and 2.85 eV, respectively, demonstrate the highest activities and Pd-Cu/C exhibits the highest stability for FAO.

1. Introduction

Fuel cells have been recognized as attractive alternative portable power sources for addressing the low energy density issue of current lithium-ion batteries [1]. Direct formic acid fuel cells (DFAFCs) have received great attention since they combine the fast fuel oxidation rate of H_2-PEMFCs and the ability of DMFCs to directly utilize the liquid fuel. Hence, DFAFCs can offer both a high power and an easy fuel handling at ambient conditions [2–4]. DFAFCs possess seven times the gravimetric energy density as compared to lithium-ion batteries [1,5]. Furthermore, unlike conventional batteries, DFAFCs can be instantaneously "recharged" by simply replacing the fuel cartridge when all the fuel is consumed. Among all metals, palladium (Pd) nanoparticles demonstrate a significantly higher activity toward formic acid oxidation (FAO) [4,6,7] by promoting "a direct pathway" where CO_2 is produced by skipping a CO intermediate step. However, the commercialization of DFAFCs has been limited by their poor long-term stability [7,8] and lower power density output than that of H_2-PEMFCs [9]. To mitigate these limitations, it is imperative to develop new anode materials with improved stability and activity toward FAO while keeping the cost down.

Studies have shown that Pd-based bimetallic catalysts have an enhanced activity and stability toward FAO as compared to that of pure Pd. For instance, Hsu et al. [10] reported that Pd-Au nanoparticles exhibit a higher electrochemical activity toward FAO, lower CO-stripping peak potential, and improved long-term durability/stability as compared to commercial Pd catalysts. Pd-Au/C catalysts with different degrees of alloying were also studied [11,12], showing that catalysts with a high degree of alloying possess a higher electrocatalytic activity and stability for FAO. Improved electrochemical performance toward FAO has also been demonstrated for nanoparticles made of Pd alloyed with Co [13,14], Cu [15,16], Ni [2,17], and Ag [18,19]. Typically, bimetallic catalysts show improved catalytic performances via one or more of the following effects: (1) a bifunctional effect [20], (2) an

* Corresponding authors.
E-mail addresses: scudiero@wsu.edu (L. Scudiero), suha@wsu.edu (S. Ha).

https://doi.org/10.1016/j.apcatb.2019.03.072
Received 27 September 2018; Received in revised form 16 February 2019; Accepted 27 March 2019
Available online 28 March 2019
0926-3373/ © 2019 Elsevier B.V. All rights reserved.

electronic effect [21], or (3) an ensemble effect [22]. In the studies mentioned above, the increase in performance of Pd-based bimetallic catalysts toward FAO was mainly attributed to an electronic effect, where the electronic properties of these catalyst surfaces are different from that of pure bulk Pd. However, both the bifunctional and ensemble effects cannot be completely neglected in those studies, because those effects are directly related to the surface composition, which for conventional bimetallic nanocatalysts differs from that of a monometallic catalyst.

To correlate the electronic effects with the FAO activity, Pd-M bimetallic nanocatalysts were synthesized in this study. These synthesized bimetallic nanoparticles (NPs) consisted of three different regions: the outermost Pd surface layer, sub-shell layer, and M core metal (M = Ru, Pt, Cu, Au, and Ag). The composition of the sub-shell layer varies from a low degree of mixing to a high degree of mixing between Pd and M metal atoms depending on the reduction potential differences between M and Pd. Our catalyst samples are ideal materials to isolate the electronic effects because their surfaces consist of 100% pure Pd. The electronic properties of the Pd surface within a Pd-M bimetallic nanocatalyst can be modified mainly by strain and ligand effects. The strain effect occurs when there is a lattice mismatch between the Pd surface layer and its underneath sub-shell layer, while the ligand effect arises due to the metal-metal bond interaction between the Pd and M metals. Both effects result in the re-distribution of their valence electrons and alter the electronic properties of the Pd surface layer. However, it is experimentally difficult to separate these two effects. Nørskov and other researchers have used a *d*-band center model to illustrate the electronic structure change produced by the addition of several different metals to a second metal. They performed density functional theory (DFT) calculations for a number of adsorbate systems and found that the *d*-band center is one of the key surface parameters that can be used to determine the strength of a chemical bond [21,23,24]. For example, when CO adsorbs on a metal surface, the 5σ and 2π* orbitals of CO hybridize with the metal *d* states [25]. As the *d*-band center shifts away from the Fermi level, the back-donation of electrons from the metal to CO is reduced, thus weakening the interaction between CO and Pd. Even though Pd-based bimetallic or trimetallic catalysts have received a significant amount of attention for the FAO reaction, to the best of our knowledge, there are only a few experimental studies relating FAO activity and *d*-band center for these Pd-based catalysts and the results are inconclusive [26,27]. Investigating such a relationship is important for improving our scientific knowledge on C1 chemistry and its dependency on the metal electronic properties.

In this work, a relationship is obtained between the electronic effect (*d*-band center) on the activity and stability of different Pd-based bimetallic nanoparticles (NPs) toward FAO. Pd-M/C nanoparticles (M = Ru, Pt, Cu, Ag, and Au) are synthesized by a successive reduction procedure. X-ray photoelectron spectroscopy (XPS) is used to probe both the core level binding energies of the M and Pd elements and the valence bands of these catalysts. TEM and line scan EDX are utilized to image the NPs and probe their chemical compositions. The electrochemical activity and stability are measured by cyclic voltammetry (CV) and chronoamperometry (CA), respectively. In addition, we quantify the amount of CO that is accumulated on the surface of the catalysts by CO stripping measurements. Finally, DFT-based calculations are performed to estimate the *d*-band center values for all the Pd-M/C NP samples by varying the mixing ratio between Pd and M metal atoms, so as to relate them to the experimentally determined *d*-band centers. Based on both the volcano plot and activity measurements, we find that the Pd-Cu/C nanocatalyst exhibits a superior activity and stability toward FAO as compared to all the other Pd-based bimetallic nanocatalysts studied in this work.

2. Experimental

2.1. Carbon supported Pd-M bimetallic nanoparticles preparation

Pd-Au/C NPs were prepared via a two-step synthesis procedure [28]. Au seeds were first synthesized according to Frens [29] then 0.001 M H_2PdCl_4 (prepared by dissolving $PdCl_2$ (≥99.99%, Sigma Aldrich) into 5 M HCl) was added. Following those initial steps, an excess amount of ice-cold ascorbic acid (8.36 mL, 0.1 M) was added drop-wise to the solution while stirring for an hour. Carbon black (Vulcan XC-72, pretreated with hydrochloric acid) was poured into the solution to prepare supported nanoparticles with a Pd loading of 10 wt%. The synthesized nanoparticles had the core@shell structure over the carbon support. After stirring the solution overnight, the Pd-Au/C NP containing solution was then centrifuged to collect the nanoparticles and the product was cleaned and dried.

Pd-Pt/C NPs were also synthesized via a two-step synthesis [30] with the same Pd loading as that for Pd-Au/C. 2.2945×10^{-4} mol of $H_2PtCl_6{\cdot}xH_2O$ (99.9%, Alfa Aesar) and 0.24 g (2.1628×10^{-3} mol) of polyvinylpyrrolidone (PVP) (MW = 5,5000, Alfa Aesar) was dissolved in 30 mL of ethylene glycol (Alfa Aesar) in a round bottom bottle. The solution was slowly heated (3 °C/min) to 160 °C under a N_2 atmosphere. After 2 h, a black colloidal solution was obtained. The PVP-Pt nanoparticles were separated by centrifuging the solution at 5000 rpm for 15 min with acetone. After discarding the suspension, the PVP-Pt NPs were washed with acetone again and re-dispersed in 20 mL of 18 MΩ Millipore water. The Pd precursor was added to the solution containing the Pt nanoparticles using the same method as described in the synthesis of Pd-Au NPs. Finally, Pd-Pt/C NPs were obtained by pouring carbon black into the solution. The same method was used to synthesize Pd-Ru/C [31] and Pd-Ag/C [30] bimetallic NPs utilizing $Ru(acac)_3$ and $AgNO_3$, respectively.

Pd-Cu/C bimetallic NPs were synthesized by the Ren method [27] with the following modification. 80 mg of $CuSO_4$ (Alfa Aesar) was added to a 20 mL solution of ethylene glycol containing 0.25 M of NaOH. The mixture was heated to 160 °C for 12 h in N_2 atmosphere. A reddish-brown colloid was obtained, indicating the formation of Cu nanoparticles. After cooling the Cu NPs in an ice bath, 0.001 M H_2PdCl_4 in 40 mL ethylene glycol and 0.7 mL concentrated H_2SO_4 were added to the Cu colloid drop-wise under ultrasonication and N_2 atmosphere to form Pd-Cu bimetallic NPs. Finally, 80 mg of acid treated Vulcan-72 carbon dispersed in 200 mL of ethylene glycol was added to the Pd-Cu colloid. After stirring overnight, the Pd-Cu/C was centrifuged and the product was cleaned and dried. Pd/C NPs was finally prepared as previously described elsewhere [32]. The solution was stirred for an additional hour, and Pd/C nanoparticles were centrifuged and washed with water.

2.2. Electrochemical analysis

The electrochemical measurements were performed on a Solartron Sl1287 Electrochemical Interface. A three-electrode system was used with a Pt mesh as the counter electrode and an Ag/AgCl (3 M KCl) electrode as the reference electrode. The glassy carbon coated with the Pd-based bimetallic catalyst was used as a working electrode. Before each measurement, high purity N_2 gas was bubbled through the electrolyte for 30 min to remove oxygen. The electrochemical active surface areas (ESA) of the Pd-based bimetallic catalysts were calculated based on the charge of the Pd-oxide stripping peak [33] and used to normalize the current densities. All the electrochemical results are referred to a standard hydrogen electrode (SHE).

Catalyst inks were prepared so as to attach the catalysts to the glassy

carbon working electrode. First, a certain amount of each catalyst was dispersed in Millipore® water to prepare 5 mg/mL suspension. Then, an appropriate amount of a 5 wt.% Nafion® solution (Dupont) was added to give a 20 wt.% Nafion® in the catalyst layer when dried. The ink was then sonicated. Finally, a total amount of 50 μL of each ink was dropped over the glassy carbon working electrode and dried under a heating lamp.

CV measurements were performed in either 0.5 M H_2SO_4 electrolyte or a mixed solution of 0.5 M H_2SO_4 and 0.5 M formic acid at a scan rate of 20 mV/s. CA measurements were conducted in an electrolyte containing 0.5 M H_2SO_4 and 0.5 M formic acid at a fixed potential of 0.26 V (SHE) for two hours. This potential is about the middle point of the onset potential and peak potential of formic acid oxidation, which is away from the mass transport limitation region. A CO stripping test was carried out in 0.5 M H_2SO_4 electrolyte at a scan rate of 20 mV/s after 2 h of CA measurements. The CO-stripping area (i.e. CO accumulation amount) for all the Pd-based bimetallic catalysts were calculated based on the area difference of the first cycle and the second cycle between 0.8 V and 1.2 V (SHE) of the CO stripping test.

2.3. X-ray photoelectron spectroscopy analysis

The XPS spectra were acquired on a Kratos AXIS-165 using a monochromatized AlKα X-ray anode (1486.7 eV). The spectrometer was calibrated against both the Au $4f_{7/2}$ peak at 84.0 eV and the Ag $3d_{5/2}$ peak at 368.3 eV. The carbon supported Pd-based bimetallic catalysts were Ar^+ sputtered to remove any adsorbed species on the sample surface. The ion gun parameters used were 15 mA @ 4 kV. The *d*-band centers were calculated by integrating the normalized first moment of the density of state (DOS) approximated by the measured N(E) [34].

2.4. Physical characterization

The size and shape of the Pd-based bimetallic catalysts were imaged by transmission electron microscopy (TEM). TEM images were obtained using a Philips CM-200 transmission electron microscope operating at 200 kV. The particle sizes are estimated by ImageJ software. The chemical compositions of the synthesized nanoparticles were further characterized by high-resolution transmission electron microscopy (HRTEM) coupled with a high-angle annular dark field scanning transmission electron microscopy (HAADF-STEM, Talos F200X) and energy dispersive X-ray spectroscopy (EDX) for line-scanning with elemental mapping at 200 kV. The samples for STEM were prepared by dispersing the NPs in ethanol and drop casting these materials on carbon film 200 mesh copper or nickel grid (CF200-Cu or CF200-Ni, Electron Microscopy Sciences).

2.5. Computational methods

The corresponding DFT-based calculations of the *d*-band centers were performed using the Vienna *Ab Initio* Simulation Package (VASP) code [35,36]. To solve for the ion-electron interactions in a periodic system, we applied the projector-augmented wave (PAW) method [37]. The generalized gradient approximation [38,39] using a Perdew-Burke-Ernzerhof (PBE) [39] functional was used to treat the exchange-correlation interactions in the Kohn-Sham equations [36]. For the plane wave basis sets, we expanded the wave functions to an energy cutoff of 400 eV.

We considered the most favorable flat surface (111) for the FCC metals (Pt, Pd, Cu, Au, Ag) and the (0001) for the HCP metal (Ru) for the simulated models (Table S1). The bimetallic system was constructed with a $p(3 \times 3)$ six-layer periodic slab with 18 Pd atoms and 36 core M atoms. We fixed the two bottom core layers at their equilibrium bulk positions and allowed the other core and shell layers to relax. In this work, the synthesized bimetallic NPs consist of three different regions: the outermost Pd surface layer, sub-shell layer, and M core metal. The composition of the sub-shell layer varies from a low degree of mixing to a high degree of mixing between Pd and M metal atoms depending on the reduction potential differences between M and Pd. To investigate the degree of mixing between Pd and M atoms for our synthesized bimetallic NPs, we have used the following procedure:

(1) Estimate the *d*-band center values of Pd-M bimetallic NPs from DFT calculations starting from a mixing ratio ($r_{M/Pd}$) between M and Pd atoms at 1/4. The $r_{M/Pd}$ value of 1/4 indicates a very low concentration of M atoms within the Pd surface layer of Pd-M bimetallic NPs.
(2) Compare the *d*-band center value from the DFT-based calculation with that of the experimental value from the XPS measurements.
(3) If the difference between the DFT-based calculation and experimental values is large, increase the value of $r_{M/Pd}$ and calculate its corresponding *d*-band center values.
(4) Repeat the steps (2) and (3) until the *d*-band center values from the DFT-based calculations and the XPS measurements are comparable.

All self-consistent field (SCF) calculations were converged to 10^{-4} eV and the forces were smaller than 0.03 eV/Å. The Brillouin zone integration was approximated by a sum over **k**-points chosen using a Monkhorst-Pack mesh [40] with a grid of $(4 \times 4 \times 1)$ **k**-points. More details on the corresponding DFT calculations can be found in the SI.

3. Results and discussion

3.1. Pd-M (M = Cu, Au, Pt, Ag, Ru) bimetallic NPs

Physical structures of synthesized NPs were characterized using a combination of various analytical tools including STEM-EDX and UV–vis measurements. Based on TEM images of the synthesized nanoparticles (Figs. 1a and S1a – S4a), the particle sizes range from 10 to 15 nm. According to the findings of Wieckowski et al., the effect of particle size on FAO activity is negligible for NPs with sizes larger than 10 nm [41,42]. Hence, we have neglected the particle size effect on the FAO catalytic performance for our synthesized nanocatalysts. In this work, the synthesized bimetallic NPs consist of three different regions: the outermost Pd surface layer, sub-shell layer, and core. The sub-shell layer is defined as the layer between “the outermost Pd surface” and “M” innermost core of the nanoparticle. Depending on which secondary M metal is used to synthesize the bimetallic NPs, the sub-shell composition ranges from pure M metal atoms to a various degree of Pd-M mixed atoms. As the composition of the sub-shell layer changes, its electronic interaction with the Pd surface would be significantly changed, which leads to an alteration of their corresponding *d*-band center values. We have investigated if there exists a direct correlation between the electrochemical activity of our synthesized bimetallic NPs toward FAO and their corresponding *d*-band center values. Even though our bimetallic NP samples have different compositions of the sub-shell layers, their outer surfaces all consisted of pure Pd atoms. Thus, we could use our bimetallic nanoparticle samples to investigate the relationship between the formic acid oxidation activity and the surface electronic properties of the Pd surface.

From Fig. 1b, the UV–vis spectra of unsupported Pd-Cu NPs clearly demonstrate that the Cu core is completely covered by the Pd surface layer. Furthermore, based on Fig. 1c, the cyclic voltammetry result shows no Cu oxidation at its redox potential of +0.25 V, which confirms that the outer most surface consists of a pure Pd surface layer. Interestingly, both line-scanning EDX data (Fig. 1d) and EDX element mapping image (Fig. 1e) of a Pd-Cu/C NP indicate that both Cu and Pd atoms are well mixed in an alloy form. Despite its EDX data, it is important to point out that the core of Pd-Cu/C NP must be rich in Cu atoms because pure Cu nanoparticles were used as a starting material. Thus, our characterization data strongly suggest that the Pd-Cu/C NP consists of the Cu-rich core, the Cu-Pd mixed sub-shell layer, and a very

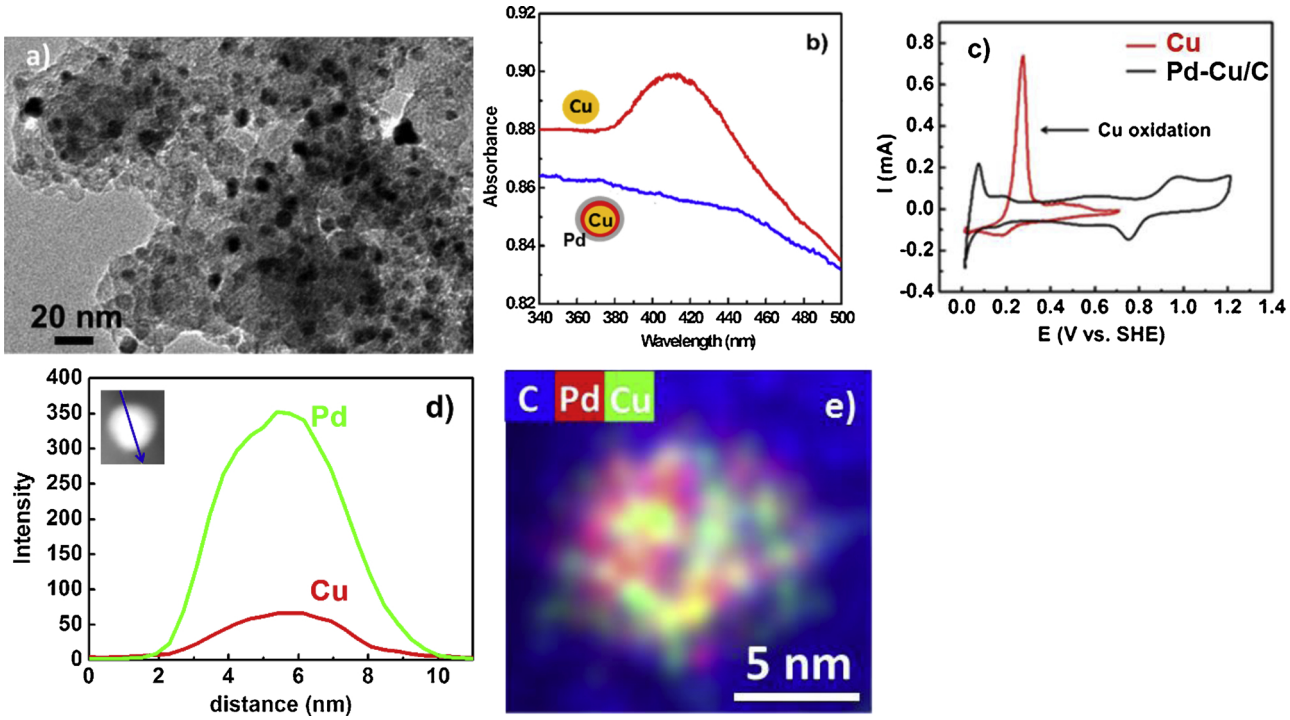

Fig. 1. Physical characterizations of Pd-Cu/C bimetallic nanoparticles. **a**) TEM images, **b**) UV–vis spectra of unsupported Cu seeds and Pd-Cu NPs, **c**) cyclic voltammetry results in 0.5 M H_2SO_4 with a scan rate of 20 mV/s, **d**) line-scanning EDX **e**) elementary mapping from EDX analysis.

thin Pd outer surface layer. This unique structure of Pd-Cu/C NP can be explained in terms of (1) the different standard electrode potential (E°) between Cu and Pd, and (2) the Cu and Pd atom diffusion at the interface. First, the E° for Pd (0.915 V) is higher than that of Cu (0.3419 V). Consequently, a spontaneous exchange reaction is taking place between Pd cations and the Cu core metal. This exchange reaction consumes part of the Cu core atoms and forms Cu cations. These Cu cations and Pd cations from the precursor solution can be reduced over the surface of the Cu core by a reducing agent to form a sub-shell structure with a high degree of mixing between the Pd and the Cu metals. The number of Pd cations would be much higher than that of the Cu cations during the synthesis process. Once all the Cu cations are reduced back to form the sub-shell structure, the Pd cations can further be deposited over this sub-shell surface to form the Pd outer shell layer. Secondly, in a previous study using a flat Pd surface thermally deposited over a Cu bulk strip, we demonstrated that Cu atoms can diffuse into the Pd lattice at the interface to form a mixed bimetallic layer and propagate to the Pd surface [43]. The calculated segregation energy (E_{seg}) [45,46] for the Pd-Cu bimetallic system is about 0.3 eV/atom (Table S2), which indicates that it is energetically favorable for Cu and Pd atoms to form and maintain its intermixed conformation. The main take-home message from the characterization of Pd-Cu/C bimetallic NPs is that they consist of a pure 100% Pd surface, while its sub-shell layer consists of a Pd-Cu mixture.

Figs. S1 and S2 display EDX elemental mapping of Pd-Ag and Pd-Ru NPs showing that both Pd and Ag or Pd and Ru atoms are present in an alloy form. However, their CV and UV–vis data suggest that the outermost layer of the Pd-Ag and Pd-Ru NPs must consist of only pure Pd atoms similar to the Pd-Cu NP. Thus, our characterization data strongly suggests that the Pd-Ag/C and Pd-Ru/C NPs consist of M-rich cores, M-Pd mixed sub-shell layers, and very thin Pd outer surface layers (M = Ag or Ru). Comparing Pd-Cu/C, Pd-Ag/C, and Pd-Ru/C NPs, Figs. S3 and S4 exhibit Pd-Au/C and Pd-Pt/C NPs with a smaller degree of mixing between Pd and M (M = Au or Pt) metals at their interfaces (i.e., a less degree of mixing within their sub-shell layers). The different sub-shell structures obtained for these Pd-Ag, Pd-Ru, Pd-Au, and Pd-Pt bimetallic NPs could be due to the different E° values for the metals studied here. The E° values for Ru^{2+}/Ru (0.455 V) and for Ag^{+}/Ag (0.7996 V) are lower than that for Pd^{2+}/Pd (0.915 V). Thus, a spontaneous exchange reaction is taking place between Pd cations and Ru (or Ag) metals similar to the Pd-Cu NP system. This exchange reaction consumes the Ru (or Ag) cores and forms its corresponding Ru (or Ag) metal cations. These Ru (or Ag) metal cations and Pd cations from the precursor solution can be reduced over the surface of Ru (or Ag) cores by the reducing agent to form the sub-shell structure with a high degree of mixing between Pd and Ru (or Ag) metals. However, the E° value for Au^{3+}/Au (1.498 V) and Pt^{2+}/Pt (1.18 V) are higher than that for Pd^{2+}/Pd. Under such conditions, only Pd^{2+} reduction occurs on Au (or Pt) core surfaces without the exchange reactions. Accordingly, their sub-shell structures consist mostly of Pd atoms with a smaller amount of mixing between Pd and their corresponding Au (or Pt) metals.

3.2. Electronic perturbations of the Pd-M bimetallic NPs

The *d*-band center values were used to estimate the degree of electronic perturbation that is induced on the Pd surface as different types of M metals are introduced for the synthesis of bimetallic Pd-M NPs. In general, the *d*-band center value is influenced by the average energy of the *d*-band, the shape of the *d*-band, and the number of electrons in the *d*-band. The surface Pd atoms are under compressive strain when the lattice parameter of the substrate is smaller than that of Pd. This compressive strain changes the average energy of the surface *d*-band, which results in a broadening of its *d*-band width and a shift of its center away from the Fermi level to maintain the band filling. This change of energy directly affects the surface chemical properties of the Pd surface, thus altering its catalytic activity. Conversely, if the substrate metal has a larger lattice constant than Pd, the *d*-band becomes narrower and its center shifts toward the Fermi level. This effect is termed the *strain effect*. In contrast, the *ligand effect* refers to a *d*-band center shift caused by a charge transfer between the Pd metal and the second metal due to their bimetallic bonding interactions. Because the lattice mismatch between Pd and the core metals used in this study

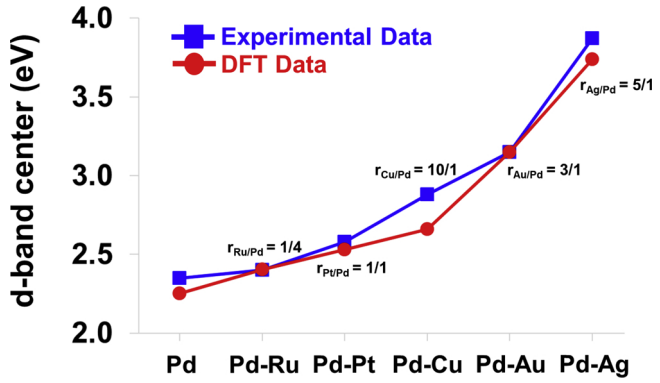

Fig. 2. The *d*-band centers for the Pd-M bimetallic nanoparticles. Experimental and DFT calculated average *d*-band centers. For DFT calculated average *d*-band centers, we varied the mixing ratios between Pd and M metal atoms ($r_{M/Pd}$) to match the average experimental *d*-band center values. The high value of $r_{M/Pd}$ indicates the high degree of mixing within the surface of Pd-M bimetallic nanoparticles, while a low value of $r_{M/Pd}$ indicates a low degree of mixing with the surface of Pd-M bimetallic nanoparticles.

varies from 0.7% for Pt, 5.2% for Ag, 5.6% for Au, 7.9% for Cu, to 8.8% for Ru, the strain effect cannot be neglected. The DFT-computed bulk lattice constants for each of these metals are given in Table S1. Experimentally, it is very challenging to separate contributions made by either the strain or the ligand effect on a given NP. Typically, DFT-based computational approaches are used to elucidate their contributions in altering the surface electronic properties of NPs [24,44].

The XPS valence band region recorded for all the Pd-M/C NPs is used to estimate the *d*-band centers. Fig. 2 shows that the *d*-band centers for all the Pd-M bimetallic NPs shift away from the Fermi level as compared to that of Pd/C. This indicates a charge transfer from the Pd (4*d*) orbitals to the empty states of the second metal, M. The order is Pd-Ag/C > Pd-Au/C > Pd-Cu/C > Pd-Pt/C > Pd-Ru/C ≅ Pd/C. Charge transfer from Pd to the M metal is also confirmed by measuring the core level binding energies (Pd 3*d* or 3*p*, and M 2*p*, 3*d* or 4*f*). As Fig. S5a –f shows, the Pd 3*d* and the 3*p* peak shift to higher core level binding energy values when forming Pd-M bimetallic NPs, while the 2*p*, 3*d*, or 4*f* peaks of most M metals shift to lower core level binding energies. This opposite core level binding energy shift trend observed for Pd and most M metals indicates that charge transfer occurs from Pd to M. In the case of Pd-Ru/C NPs, both Pd 3*d* and Ru 3*d* lines shift negligibly as compared to the parent atoms suggesting that an insignificant charge transfer takes place between Pd and Ru. The magnitude of the core level binding energy shifts for Pd follows the order: Pd-Ag/C ≅ Pd-Au/C > Pd-Cu/C > Pd-Pt/C > Pd-Ru/C. In general, such order agrees with the *d*-band center shift for the same Pd-M bimetallic nanoparticle samples.

To determine the direction of charge transfer, one needs to consider the electronegativity values of Pd and M metals as well as their electronic configurations. For the Pd-Ru/C NP sample, both the Ru and Pd have the same electronegativity (χ = 2.20). Since their affinity to gain additional electrons are about the same, there is no driving force for the charge transfer between the Ru and Pd atoms. Based on this argument, charge transfers from Pd to Pt and from Pd to Au are expected to occur because the electronegativity of both Pt (2.28 eV) and Au (2.45 eV) are higher than that of Pd (2.20 eV). Such a charge transfer process decreases the population of the 4*d* band of the Pd surface for the Pd-Pt/C and Pd-Au/C bimetallic NP systems, resulting in a shifted *d*-band center away from the Fermi level as shown in Fig. 2.

On the other hand, the electronegativity of Cu and Ag is lower than that of Pd with values of 1.90 and 1.93, respectively. Using the same electronegativity argument, a charge transfer should occur from Cu (or Ag) to Pd shifting the *d*-band center of Pd-Cu/C (or Pd-Ag/C) bimetallic NPs toward the Fermi level. However, our experimental data demonstrates that their *d*-band centers shift in the opposite direction. Therefore, the electronegativity argument used above could not be the main effect that determines the direction of charge transfer for Pd-Cu/C and Pd-Ag/C bimetallic NPs. For these two metals, we can argue that the electronic configuration effect could outplay the electronegative effect since both metals have filled *d* orbitals and a half-filled *s* orbital ([Ar]$3d^{10}4s^1$ for Cu, and [Kr]$4d^{10}5s^1$ for Ag) that can give or receive an electron. Pd has a fully filled 4*d* orbital, i.e. [Kr]$4d^{10}$. It is therefore more energetically favorable for the electrons in the 4*d* band of Pd to transfer into the empty states of the Cu and Ag metals. The reduced electron population in the 4*d* band of Pd results in a shift of the *d*-band center away from the Fermi level. Hence, for Pd-Cu/C and Pd-Ag/C NPs, it appears that their electronic configuration plays a greater role than their electronegativity for determining the direction of the valence electron transfer.

In summary, a full understanding of the electronic structure of our synthesized bimetallic NPs requires a careful consideration of several properties such as the electronegativity and orbital filling. Nevertheless, our valence XPS data demonstrates that the electronic properties of Pd-Ag/C NPs change the most followed by Pd-Au/C, Pd-Cu/C, Pd-Pt/C, Pd-Ru/C and Pd/C NPs. Both Pd-Ru/C and Pd/C NPs show a very similar electronic structure.

3.3. Electrochemical performance of formic acid oxidation on Pd-M bimetallic NPs

The electrochemical activity of these carbon supported Pd-M bimetallic catalysts is measured by cyclic voltammetry and their results are summarized in Fig. 3. The maximum current density for Pd-Ag/C, Pd-Au/C, Pd-Cu/C, Pd-Pt/C, Pd-Ru/C, and Pd/C are 0.8, 1.8, 3.2, 3.3, 1.5 and 0.9 mA/cm^2, respectively. The Pd-Pt/C and Pd-Cu/C catalysts show the highest activity toward FAO. Comparing to Pd/C, Pd-Cu/C shows the best FAO activity with 64 wt.% Pd metal reduction. A comparison between the results obtained in this study and other researchers are listed in Table S3 in the Supporting Information. According to Table S3, our Pd-Cu/C NP sample demonstrates a higher activity than the previously studied bimetallic or trimetallic NPs for FAO. For example, Zhu et al. synthesized Pd-Sn-Ag/C trimetallic NPs and showed a peak current density of 2.59 mA/cm^2. Lu et al. prepared Pd-Ru/C bimetallic NP and demonstrated a peak current of 4.1 mA/cm^2. It seems that Lu et al. performance is higher than our Pd-Cu/C bimetallic NP. However, it is important to point out that they used an expensive Ru noble metal (instead of inexpensive Cu) as the second metal to improve the performance of Pd. Furthermore, they used 120% more Pd atoms than our

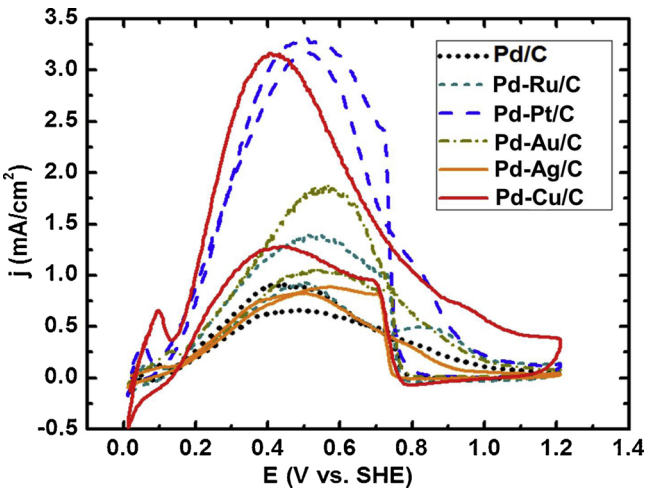

Fig. 3. Electrochemical activity of Pd-M bimetallic nanoparticles toward formic acid oxidation. Cyclic voltammetry of Pd/C and Pd-M bimetallic nanoparticles in 0.5 M H_2SO_4 with 0.5 M formic acid, scan rate: 20 mV/s.

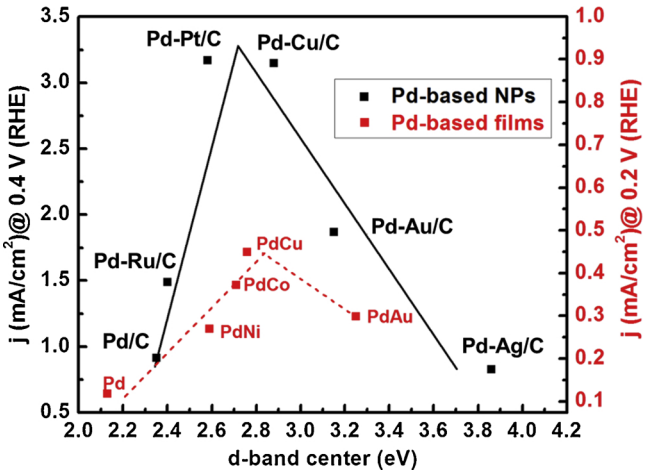

Fig. 4. Electronic structure effects of the Pd surface on the formic acid oxidation (FAO) electrochemical activity of Pd/C and Pd-M bimetallic nanoparticles (solid line) and thin Pd-M bimetallic films[47] (dash line). A Volcano shape relationship is obtained between the activity toward FAO and the *d*-band center for the materials under consideration.

Pd-Cu/C NP sample to obtain its peak current. If we normalize the activity of our Pd-Cu/C NP based on the amount of Pd used to synthesize the NP, its peak current density becomes 25 mA/mg of Pd at 0.4 V vs. RHE, which is one of the best performances that can be found in the literature.

Fig. 4 displays a plot of the electrochemical activity toward FAO versus the *d*-band center for all synthesized Pd-M bimetallic catalysts. A volcano shape relationship is obtained. As the *d*-band center shifts away from the Fermi level, the FAO activity over the Pd-M bimetallic catalysts increases quasi-linearly until it reaches a *d*-band center value between 2.58 and 2.85 eV for Pd-Pt/C and Pd-Cu/C NPs, respectively, then the activity decreases as the *d*-band center shifts further away from the Fermi level. A similar volcano shape relationship was also demonstrated in a previous work on Pd-based bimetallic thin films (See Fig. 4) [47]. For these thin Pd-M bimetallic films, only electronic effects are expected to play a major role in altering their surface electrocatalytic activities. Hence, a similar volcano shape relationship between thin films and bimetallic catalysts strongly suggests that electronic effects are the main contributor to the electrochemical improvement toward FAO for the Pd-M bimetallic NPs investigated in this work.

It has been widely accepted that the FAO reaction on Pd can proceed by the direct pathway with formate (HCOO) as its key intermediate as shown in Eqs. (1) and (2):

$$HCOOH \rightarrow HCOO_{ad} + H^+ + e^- \quad (1)$$

$$HCOO_{ad} \rightarrow H^+ + e^- + CO_2 \quad (2)$$

It is known that formate species binds to the Pd surface with a Pd-O bond to form a monodentate or bidentate configuration [48,49]. Based

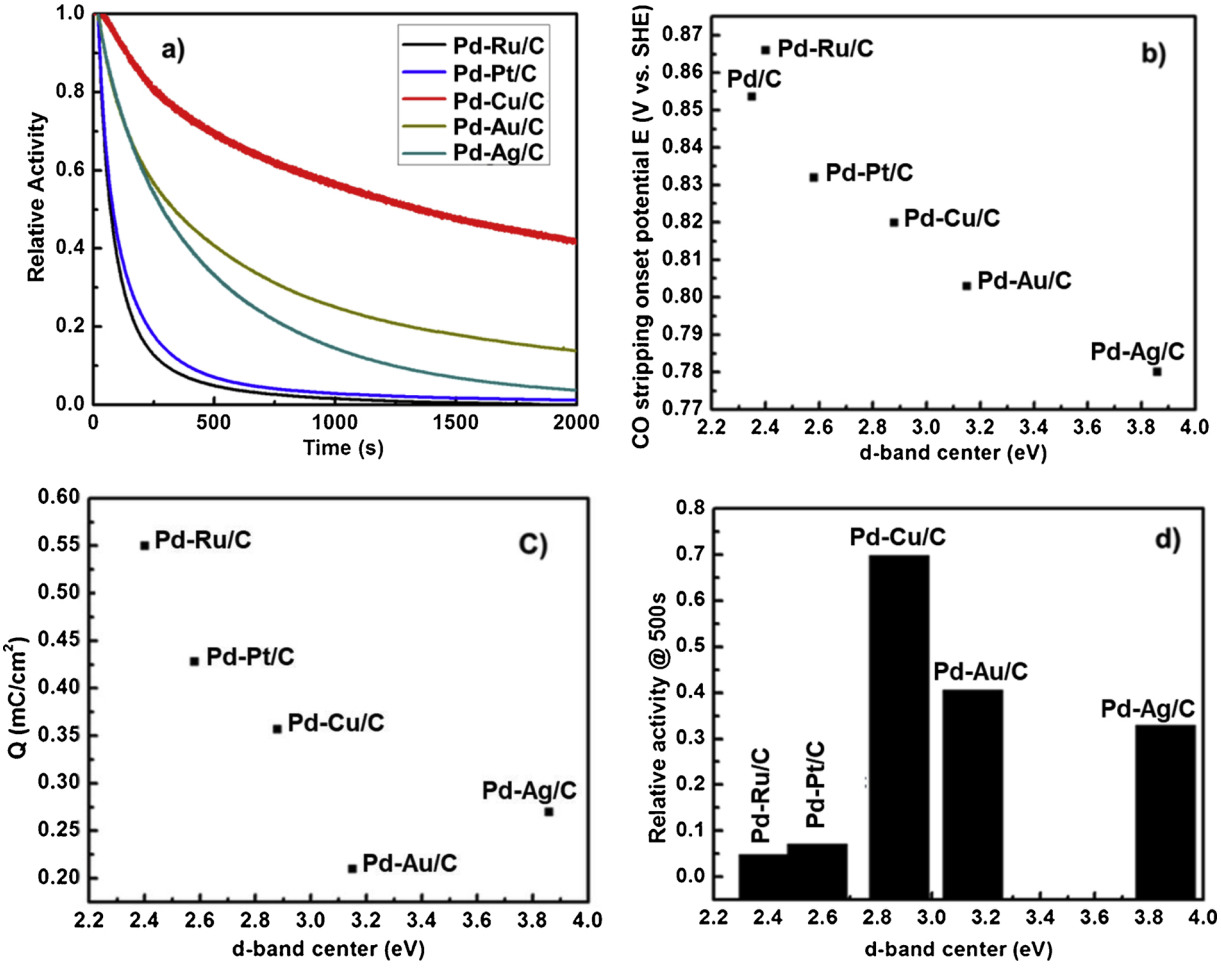

Fig. 5. Electrochemical stability of Pd-M bimetallic nanoparticles toward FAO. **a**) Chronoamperometry data of Pd-M bimetallic nanoparticles in 0.5 M H_2SO_4 with 0.5 M formic acid at a fixed potential of 0.26 V (SHE). **b**) Relationship between the CO stripping peak onset potential and *d*-band center for the Pd-M bimetallic nanoparticles. **c**) Relationship between the CO stripping area (CO accumulation amount) and *d*-band center for the Pd-M bimetallic nanoparticles, **d**) Relationship between the relative activity @ 500 s and *d*-band center for the Pd-M bimetallic nanoparticles.

on the calculations of Nørskov et al. [25,50–52], the HCOO-Pd bond should be weakened as the *d*-band center shifts away from the Fermi level. According to the Sabatier principle [23], the highest catalytic activity is observed when the bond strength between the key intermediate species and the surface is not "too strong" and not "too weak". If the bond strength is too weak, the key intermediate species is not going to form. If the bond strength is too strong, the key intermediate species can poison the surface by blocking the active sites for additional reactants to react. With a *d*-band center of 2.35 eV, the Pd/C catalyst offers a high degree of overlap between its *d*-band and the orbitals of the adsorbed formate species [26], which leads to a "too strong" bond strength between the $HCOO_{ad}$ and Pd surface atoms. Based on this argument, for the Pd/C sample, Eq. (2) becomes the rate-limiting step for the FAO reaction. Consequently, the FAO activity increases as the *d*-band center shifts away from the Fermi level and the maximum FAO activity is achieved when the *d*-band center reaches a value between 2.58 and 2.85 eV for the Pd-Pt/C and Pd-Cu/C NPs. However, as seen for Pd-Au/C and Pd-Ag/C NPs, the FAO activity decreases as the *d*-band center shifts beyond 2.85 eV. These further shifts of the *d*-band center from the Fermi level contribute to the weakening of the HCOO-Pd bond to a point that it limits the adsorption of HCOO on the Pd surface. Hence, Eq. (1) becomes a rate-limiting step for the complete oxidation of formic acid.

The long-term stability of Pd-based catalysts for the FAO is another technical challenge [8,53]. Results from several studies suggest that the CO_{ad} could accumulate *slowly* on the Pd surface during the oxidation of formic acid via the formic acid dehydration reaction pathway (Eq. (3)) or CO_2 reduction (Eq. (4)) [48,54].

$$HCOOH \rightarrow CO_{ad} + H_2O \quad (3)$$

$$CO_2 + 2H^+ + e^- \rightarrow CO_{ad} + H_2O \quad (4)$$

Fig. 5a displays CA measurements that evaluate the stability of the Pd-M bimetallic NPs for FAO. Based on those measurements, the stability of Pd-M bimetallic NPs increases in the following order: Pd-Ru/C < Pd-Pt/C < Pd-Ag/C < Pd-Au/C < Pd-Cu/C. As the *d*-band center shifts away from the Fermi level, a lower number of electrons are available for establishing a strong Pd−CO bond, which reduces the amount of CO produced on the Pd surface via the dehydration pathway of Eq. (3) and CO_2 reduction of Eq. (4). Following the CA measurements, CO stripping experiments were immediately performed to investigate the relationship between the CO binding energy as well as the accumulated total amount of CO over the Pd surface and the surface *d*-band center. Typically, the onset potential of CO stripping (i.e., the potential at which CO oxidation starts) decreases as its surface binding energy decreases. Fig. 5b plots the CO stripping onset potential as a function of the *d*-band center, and Fig. 5c displays the total CO accumulation amount as a function of the *d*-band center. Among Pd-Ru/C, Pd-Pt/C and Pd-Cu/C NP samples, Pd-Cu/C NPs show the highest stability with the lowest onset potential of CO stripping and the smallest amount of CO accumulation followed by Pd-Pt/C and Pd-Ru/C NPs. Thus, the CO poisoning mechanism matches well with the stability data for Pd-Ru/C, Pd-Pt/C and Pd-Cu/C NPs. On the other hand, the same CO poisoning mechanism fails in describing the stability data of both Pd-Au/C and Pd-Ag/C NP samples. Based on the CO poisoning mechanism, Pd-Au/C and Pd-Ag/C NPs should show the highest stability for FAO due to their lowest onset potential values and the smallest CO accumulation amounts among all NP samples that we have tested. However, they exhibit much lower electrochemical stabilities than that measured for Pd-Cu/C NPs (Fig. 5a and d). This demonstrates that the CO poisoning is not the major source of the catalyst deactivation for these two NP samples. Further studies are required to provide a clear deactivation mechanism for both Pd-Au/C and Pd-Ag/C NPs toward FAO. In summary, among all the nanoparticles studied in this work, the Pd-Cu/C catalyst displays both a superior electrochemical activity and stability toward the oxidation of formic acid, which makes it a promising anode catalyst for DFAFCs.

4. Conclusions

Pd-M bimetallic catalysts (M = Ru, Pt, Cu, Au, and Ag) were successfully synthesized and their physical properties were analyzed by TEM, line scan EDX, CV and UV–vis methods. XPS valence band and core-level spectra confirm that charge transfer occurs from Pd to M for most NPs, resulting in an upshifted *d*-band center from the Fermi level with the following order: Pd-Ru/C < Pd-Pt/C < Pd-Cu/C < Pd-Au/C < Pd-Ag/C. In addition, DFT-based calculations and EDX mapping results provide insights into the composition and geometric structure of the synthesized nanocatalysts studied in this work. In summary, a relationship between the FAO activity and the *d*-band center for these nanocatalysts displays a volcano shape showing the highest activity toward FAO for a *d*-band center value ranging from 2.58 to 2.85 eV as seen for Pd-Pt/C and Pd-Cu/C. In the case of the Pd-Cu/C NP sample, it demonstrates both the highest activity and enhanced stability toward the FAO, while reducing the noble metal content by 64 wt.% as compared to the Pd/C NPs. Therefore, the Pd-Cu/C NP is a very promising and an inexpensive catalyst that can be used as the anode material to build cost-efficient DFAFCs with much-improved power density and long-term stability for alternative portable power sources.

Acknowledgements

The experimental work was funded by the National Science Foundation under Agreement CBET-1033601, DMR-9503304 and CHE-1048600. F.C. and J.-S.M. were primarily funded by the U.S. Department of Energy, Office of Basic Energy Science, Division of Chemical Sciences, Biosciences and Geosciences (DE-SC0014560) for the corresponding DFT-based calculations. We would like also to thank the Murdock Charitable Trust for its financial support in upgrading our existing XPS instrument. The Pacific Northwest National Laboratory is operated by Battelle for the U.S. DOE.

Appendix A. Supplementary data

Supplementary material related to this article can be found, in the online version, at doi:https://doi.org/10.1016/j.apcatb.2019.03.072.

References

[1] O.Z. Sharaf, M.F. Orhan, Renew. Sustain. Energy Rev. 32 (2014) 810–853.
[2] S.L. Wang, J.F. Chang, H.G. Xue, W. Xing, L.G. Feng, Chemelectrochem 4 (5) (2017) 1243–1249.
[3] H. Xu, B. Yan, S. Li, J. Wang, C. Wang, J. Guo, Y. Du, ACS Sustain. Chem. Eng. 6 (1) (2018) 609–617.
[4] S.K. Yao, G.Q. Li, C.P. Liu, W. Xing, J. Power Sources 284 (2015) 355–360.
[5] C. Rice, S. Ha, R.I. Masel, A. Wieckowski, J. Power Sources 115 (2) (2003) 229–235.
[6] Z.L. Liu, L. Hong, M.P. Tham, T.H. Lim, H.X. Jiang, J. Power Sources 161 (2) (2006) 831–835.
[7] S.M. Baik, J. Han, J. Kim, Y. Kwon, Int. J. Hydrogen Energy 36 (2011) 14719–14724.
[8] Y. Zhou, J.G. Liu, J.L. Ye, Z.G. Zou, J.H. Ye, J. Gu, T. Yu, A.D. Yang, Electrochim. Acta 55 (17) (2010) 5024–5027.
[9] S. Ha, R. Larssen, Y. Zhu, R.I. Masel, Fuel Cells 4 (4) (2004) 337–343.
[10] C. Hsu, C. Huang, Y. Hao, F. Liu, Electrochem. commun. 23 (2012) 133–136.
[11] G. Zhang, Y. Wang, X. Wang, Y. Chen, Y. Zhou, Y.-W. Tang, L. Lu, J. Bao, T. Lu, Appl. Catal. B-Environ. 102 (2011) 614–619.
[12] Y.G. Suo, I.M. Hsing, Electrochim. Acta 56 (5) (2011) 2174–2183.
[13] V. Mazumder, M. Chi, M.N. Mankin, Y. Liu, O. Metin, D. Sun, K.L. More, S. Sun, Nano Lett. 12 (2012) 1102–1106.
[14] A. Shafaei Douk, H. Saravani, M. Noroozifar, J. Alloys Compd. 739 (2018) 882–891.
[15] B. Yan, C. Wang, H. Xu, K. Zhang, S. Li, Y. Du, Chempluschem 82 (8) (2017) 1121–1128.
[16] Y. Suo, Y. Guo, C. Rong, Z. Zhang, G. Hu, Int. J. Electrochem. Sci. 12 (5) (2017) 3561–3575.
[17] K.Q. Ding, L. Liu, Y.L. Cao, X.R. Yan, H.G. Wei, Z.H. Guo, Int. J. Hydrogen Energy 39 (14) (2014) 7326–7337.
[18] G.-T. Fu, C. Liu, Q. Zhang, Y. Chen, Y.-W. Tang, Sci. Rep. (2015) 5.
[19] Y.Y. Jiang, Y.Z. Lu, D.X. Han, Q.X. Zhang, L. Niu, Nanotechnology 23 (10) (2012).

[20] C.J. Pelliccione, E.V. Timofeeva, J.P. Katsoudas, C.U. Segre, J. Phys. Chem. C 117 (37) (2013) 18904–18912.
[21] J.R. Kitchin, J.K. Nørskov, M.A. Barteau, J.G. Chen, Phys. Rev. Lett. 93 (15) (2004).
[22] Y. Ma, T. Diemant, J. Bansmann, R.J. Behm, Phys. Chem. Chem. Phys. 13 (2011) 10741–10754.
[23] A.J. Medford, A. Vojvodic, J.S. Hummelshoj, J. Voss, F.A. Pederson, F. Studt, T. Bligaard, A. Nilsson, J.K. Nørskov, J. Catal. 328 (2015) 36–42.
[24] A. Khorshidi, J. Violet, J. Hashemi, A.A. Peterson, Nat. Catal. 1 (4) (2018) 263–268.
[25] F. Gao, D.W. Goodman, Chem. Soc. Rev. 41 (24) (2012) 8009–8020.
[26] V. Celorrio, P.M. Quaino, E. Santos, J. Florez-Montano, J.J.L. Humphrey, O. Guillen-Villafuerte, D. Plana, M.J. Lazaro, E. Pastor, D.J. Fermin, ACS Catal. 7 (3) (2017) 1673–1680.
[27] M. Ren, Y. Zhou, F. Tao, Z. Zou, D.L. Akins, H. Yang, J. Phys. Chem. C 118 (24) (2014) 12669–12675.
[28] L. Lu, H. Wang, S. Xi, H. Zhang, J. Mater. Chem. 12 (2001) 156–158.
[29] G. Frens, Nat. Phys. Sci. 241 (1973) 20–22.
[30] K. Tedsree, T. Li, S. Jones, C.W.A. Chan, K.M.K. Yu, P.A.J. Bagot, E.A. Marquis, G.D.W. Smith, S.C.E. Tsang, Nat. Nanotechnol. 6 (5) (2011) 302–307.
[31] S. Alayoglu, A.U. Nilekar, M. Mavrikakis, B. Eichhorn, Nat. Mater. 7 (4) (2008) 333–338.
[32] R. Larsen, S. Ha, J. Zakzeski, R.I. Masel, J. Power Sources 157 (1) (2006) 78–84.
[33] P.N. Bartlett, B. Gollas, S. Guerin, J. Marwan, Phys. Chem. Chem. Phys. 4 (15) (2002) 3835–3842.
[34] V.R. Stamenkovic, B.S. Mun, M. Arenz, K.J.J. Mayrhofer, C.A. Lucas, G.F. Wang, P.N. Ross, N.M. Markovic, Nat. Mater. 6 (3) (2007) 241–247.
[35] G. Kresse, J. Hafner, Phys. Rev. B 47 (1) (1993) 558–561.
[36] G. Kresse, J. Furthmüller, Comput. Mater. Sci. 6 (1) (1996) 15–50.
[37] M.C. Payne, T.A. Arias, J.D. Joannopoulos, Rev. Mod. Phys. 64 (4) (1992) 1045–1097.
[38] J. White, D. Bird, Phys. Rev. B 50 (7) (1994) 4954–4957.
[39] J.P. Perdew, K. Burke, M. Ernzerhof, Phys. Rev. Lett. 77 (18) (1996) 3865–3869.
[40] H.J. Monkhorst, J.D. Pack, Phys. Rev. B 13 (12) (1976) 5188–5192.
[41] W.P. Zhou, A. Lewera, R. Larsen, R.I. Masel, P.S. Bagus, A. Wieckowski, J. Phys. Chem. B 110 (27) (2006) 13393–13398.
[42] Y. Suo, I.M. Hsing, Electrochim. Acta 55 (1) (2009) 210–217.
[43] S.Z. Hu, S. Ha, L. Scudiero, Electrochim. Acta 105 (2013) 362–370.
[44] W. Tang, G. Henkelman, J. Chem. Phys. (2009) 130.
[45] L. Vitos, A.V. Ruban, H.L. Skriver, J. Kollar, Surf. Sci. 411 (1-2) (1998) 186–202.
[46] A.U. Nilekar, A.V. Ruban, M. Mavrikakis, Surf. Sci. 603 (2009) 91–96.
[47] S.Z. Hu, L. Scudiero, S. Ha, Electrochem. commun. 38 (2014) 107–109.
[48] Y.Y. Wang, Y.Y. Qj, D.J. Zhang, C.B. Liu, J. Phys. Chem. C 118 (4) (2014) 2067–2076.
[49] T.L. Silbaugh, E.M. Karp, C.T. Campbell, J. Am. Chem. Soc. 136 (10) (2014) 3964–3971.
[50] V. Stamenkovic, B.S. Mun, K.J.J. Mayrhofer, P.N. Ross, N.M. Markovic, J. Rossmeisl, J. Greeley, J.K. Nørskov, Angew. Chem. Int. Ed. Engl. 45 (18) (2006) 2897–2901.
[51] B. Hammer, Y. Morikawa, J.K. Nørskov, Phys. Rev. Lett. 76 (12) (1996) 2141–2144.
[52] J.R. Kitchin, J.K. Nørskov, M.A. Barteau, J.G. Chen, J. Chem. Phys. 120 (21) (2004) 10240–10246.
[53] X.M. Wang, Y.Y. Xia, Electrochem. Commun. 10 (10) (2008) 1644–1646.
[54] J.Y. Wang, H.X. Zhang, K. Jiang, W.B. Cai, J. Am. Chem. Soc. 133 (38) (2011) 14876–14879.